

# Cilia metasurfaces for electronically programmable microfluidic manipulation

<https://doi.org/10.1038/s41586-022-04645-w>

Received: 19 November 2021

Accepted: 14 March 2022

Published online: 25 May 2022

 Check for updates

Wei Wang<sup>1,2</sup>, Qingkun Liu<sup>1</sup>, Ivan Tanasijevic<sup>3</sup>, Michael F. Reynolds<sup>1</sup>, Alejandro J. Cortese<sup>4</sup>, Marc Z. Miskin<sup>5</sup>, Michael C. Cao<sup>6,7</sup>, David A. Muller<sup>6,7</sup>, Alyosha C. Molnar<sup>4</sup>, Eric Lauga<sup>3</sup>, Paul L. McEuen<sup>1,7,8</sup> & Itai Cohen<sup>1,7,8</sup>

Ciliary pumping is a powerful strategy used by biological organisms to control and manipulate fluids at the microscale. However, despite numerous recent advances in optically, magnetically and electrically driven actuation, development of an engineered cilia platform with the potential for applications has remained difficult to realize<sup>1–6</sup>. Here we report on active metasurfaces of electronically actuated artificial cilia that can create arbitrary flow patterns in liquids near a surface. We first create voltage-actuated cilia that generate non-reciprocal motions to drive surface flows at tens of microns per second at actuation voltages of 1 volt. We then show that a cilia unit cell can locally create a range of elemental flow geometries. By combining these unit cells, we create an active cilia metasurface that can generate and switch between any desired surface flow pattern. Finally, we integrate the cilia with a light-powered complementary metal–oxide–semiconductor (CMOS) clock circuit to demonstrate wireless operation. As a proof of concept, we use this circuit to output voltage pulses with various phase delays to demonstrate improved pumping efficiency using metachronal waves. These powerful results, demonstrated experimentally and confirmed using theoretical computations, illustrate a pathway towards fine-scale microfluidic manipulation, with applications from microfluidic pumping to microrobotic locomotion.

Ciliary pumping is one of the most important and ubiquitous fluidic transport methods in the microscopic world<sup>7–13</sup>; however, it is challenging to engineer artificial cilia platforms that can be widely adopted<sup>2,14</sup>. Several pioneering studies have demonstrated methods for fabricating artificial cilia with actuation based on pressure<sup>15</sup>, light<sup>16,17</sup>, electrostatic<sup>18</sup> and magnetic<sup>19,20</sup> interactions; however, these systems have severe limitations. For example, cilia that are pressure-driven or optically driven can be locally actuated. These systems have, however, been challenging to implement at the microscale<sup>6,15</sup>. Moreover, there is no clear pathway for integrating them with mobile micromachines while retaining local actuation<sup>21</sup>. Electrostatically actuated cilia has been shown as a powerful method for rapid pumping and mixing<sup>18</sup>. The actuators demonstrated thus far are, however, driven by large voltages. This large voltage makes them incompatible with complementary metal–oxide–semiconductor (CMOS) electronics for untethered control. In addition, they cannot be operated in aqueous solutions, owing to hydrolysis at voltages above approximately 1.2 V. Finally, there has been much excitement about making artificial cilia out of magnetically responsive materials. Various groups have demonstrated pumping<sup>5</sup>, metachronal waves<sup>4,22,23</sup> and mixing<sup>24</sup>. In such magnetic systems, however, it is difficult to localize the actuation or change the magnetization of the cilia in situ to reconfigure the flows. Thus, to obtain wide adoption for this transport method in

engineered systems, there remains a critical need for development of novel artificial cilia platforms.

Here we show that recently developed surface electrochemical actuators<sup>25,26</sup> can be used to overcome many of these challenges. Each artificial cilium consists of a lithographically fabricated strip that is approximately 50  $\mu\text{m}$  long, 5  $\mu\text{m}$  wide and only about 10 nm thin, attached to the substrate at one end, as shown in Fig. 1a. The strip comprises a 7-nm-thick platinum (Pt) thin film capped on one side by a passive layer of titanium (Ti) (Fig. 1a, left; see Methods and Extended Data Fig. 1 for the fabrication process). Actuation of the artificial cilium in phosphate-buffered saline (PBS; 1 $\times$ , pH 7.45) is induced by raising its potential to about 1 V relative to the Ag/AgCl reference electrode, triggering electrochemical oxidation of the exposed Pt surface while avoiding bubble formation. The oxidation expands the Pt surface<sup>26</sup> and causes the actuator to bend (Fig. 1a, red reaction pathway, left  $\rightarrow$  right). Applying a voltage of approximately  $-0.2$  V reduces the Pt film, which returns the actuator to its initial state (Fig. 1a, blue reaction pathway, right  $\rightarrow$  left). The current density is approximately 1  $\text{mA cm}^{-2}$  (Extended Data Fig. 2), which means that a 1 cm  $\times$  1 cm device fully covered by artificial cilia would only consume about 1 mW of power at a sweep rate of 1  $\text{V s}^{-1}$ . To prevent twisting of the actuator we pattern three horizontal polymer pads spaced at 15- $\mu\text{m}$  intervals along each cilium.

<sup>1</sup>Laboratory of Atomic and Solid State Physics, Cornell University, Ithaca, NY, USA. <sup>2</sup>Sibley School of Mechanical and Aerospace Engineering, Cornell University, Ithaca, NY, USA. <sup>3</sup>Department of Applied Mathematics and Theoretical Physics, University of Cambridge, Cambridge, UK. <sup>4</sup>Department of Electrical and Computer Engineering, Cornell University, Ithaca, NY, USA. <sup>5</sup>Department of Electrical and Systems Engineering, University of Pennsylvania, Philadelphia, PA, USA. <sup>6</sup>School of Applied and Engineering Physics, Cornell University, Ithaca, NY, USA. <sup>7</sup>Kavli Institute at Cornell for Nanoscale Science, Cornell University, Ithaca, NY, USA. <sup>8</sup>Department of Physics, Cornell University, Ithaca, NY, USA. ✉e-mail: ww459@cornell.edu; ql59@cornell.edu; itai.cohen@cornell.edu

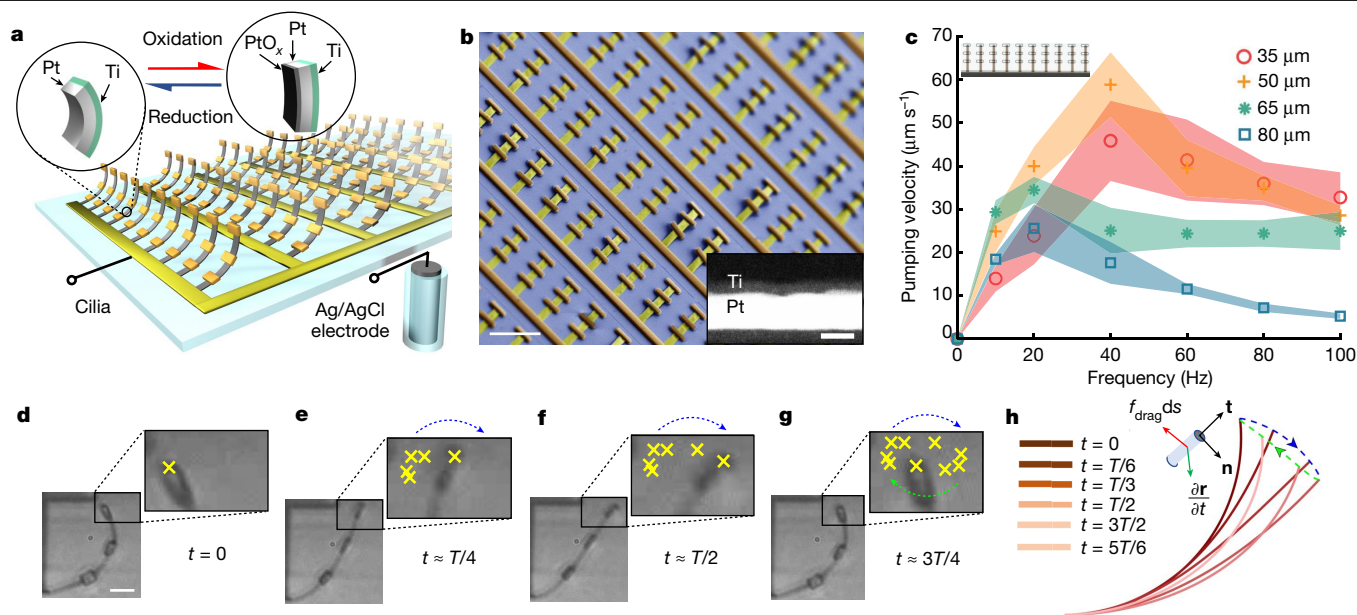


**Fig. 1 | Artificial cilia based on surface electrochemical actuators.** **a**, Each cilium consists of a thin surface electrochemical actuator made of a platinum strip capped on one side by a titanium film<sup>25,26</sup>. **b**, SEM image of released artificial cilia arrays with each row connected by a single busbar. A STEM image of a cilium cross-section showing the platinum (white) and titanium (black) is presented in the bottom-right inset. **c**, Experimental results for pumping velocity versus frequency for a single cilia array such as the one shown in the top-left inset. The velocities are obtained for tracer particles in a 20 μm by 20 μm by 5 μm region surrounding the cilia tips. The data points show the mean pumping velocity over five different measurements at different actuation frequencies and the shaded regions indicate the standard deviation. The highest pumping velocity of 60 μm s<sup>-1</sup> is achieved for cilia of length 50 μm and a driving frequency of 40 Hz. **d–g**, Non-reciprocal motion of one 50-μm-long

cilium driven at 40 Hz. Magnified trajectories of the tip are shown at the top right.  $T$  is the period of actuation cycle. The yellow cross symbols indicate the positions of the cilium tip at times  $t = 0$  (**d**),  $t = T/4$  (**e**),  $t = T/2$  (**f**) and  $t = 3T/4$  (**g**), corresponding to different moments in the stroke cycle. We observe that the trajectory traced out by the tip is elliptical, indicating that the cilium is executing a non-reciprocal stroke capable of driving flows even at low Reynolds numbers. **h**, Numerical simulation of a cilium stroke cycle. The colours, dark to light, indicate the cilium morphology at different moments during the stroke cycle. The blue and green arrows indicate the tip trajectory during the expansion and contraction of the cilium upper surface. We find excellent correspondence between the simulated cilium shapes and the experimentally determined cilium morphologies in **d–g**. Scale bars: 50 μm (**b**), 5 nm (**b**, inset), 10 μm (**d**).

Because surface electrochemical actuators can be lithographically fabricated, millions could be fabricated on one 4-inch wafer; the actuation of cilia arrays with 80 cilia is shown in Supplementary Video 1. We show a scanning electron microscope (SEM) image of a small region of the released cilia in Fig. 1b. Each cilia array is connected through a busbar that enables independent actuation. In the bottom-right inset of Fig. 1b, we show an annular dark-field scanning transmission electron microscope (STEM) image of a fabricated cilium cross-section. This ciliary platform enables an advantageous combination of features including local electrical actuation, operation in aqueous solutions, and compatibility with CMOS electronics to generate complex switchable microfluidic manipulations.

A critical requirement for these cilia to function at the low Reynolds numbers characteristic of microscale flows is that they should be sufficiently compliant so that viscous forces acting on them induce shape changes that break time-reversal symmetry<sup>27–29</sup>. To determine the optimal cilia length and conditions for pumping, we fabricate an artificial cilia array consisting of 10 cilia spaced horizontally by half a cilium length (Fig. 1c, top left) and use tracer particles to determine the pumping speed as a function of the frequency of the applied voltage for cilia with four different lengths (35 μm, 50 μm, 65 μm and 80 μm). These lengths are chosen so that the cilia whose Young's modulus is approximately 150 GPa operating in water with viscosity of about 10<sup>-3</sup> Pa·s achieves a dimensionless Sperm number (characterizing the ratio of viscous to elastic stresses acting on each cilium)<sup>30</sup> greater than one at a frequency of a few Hz. We find that for one array with this cilia design, a maximal pumping speed of about 60 μm s<sup>-1</sup> is achieved when the cilia are 50 μm long and are driven at 40 Hz, corresponding to a Reynolds number of approximately 2 × 10<sup>-3</sup>. This pumping speed could

be maintained for thousands of cycles (Extended Data Fig. 3). Further, for all cilia lengths, optimal pumping is achieved for a Sperm number range between 3 and 5 (Extended Data Fig. 4d). This range of Sperm numbers reflects the conditions under which the area swept by a cilium is largest<sup>31</sup> (Extended Data Fig. 4c), and is consistent with classical work on artificial microswimmers<sup>30,32</sup> and biological cilia<sup>33</sup>.

To further explain the origin of the time-reversal symmetry breaking, we observe the full stroke pattern for a single cilium. Specifically, we built a hinged stage so that we could observe a cilium's pumping stroke from the side (Fig. 1d–g, Extended Data Fig. 5 and Supplementary Video 2). We capture the locations of the cilium tip over a full stroke and find that it does indeed sweep out an elliptical trajectory, indicating non-reciprocal motion. This motion results from the interplay between viscous forces and the elasticity of the cilia. Specifically, the forced chemical reactions induce internal elastic stresses. The relaxation of elastic stresses starts from the free end and propagates towards the clamped end on a timescale controlled by the viscous forces, usually referred to as the elastohydrodynamic timescale. In our devices, the period of the forcing is set to be comparable with the elastohydrodynamic timescale of the cilia resulting in a continuous lag between the tip (free end) and the root (clamped end) of the cilia, which gives rise to non-reciprocal motion. Theoretical calculations based on a numerical implementation of resistive force theory<sup>34–36</sup>, show very similar trajectories and corresponding cilium shapes (Fig. 1h and Supplementary Video 3). The agreement between the simulations and experiments indicates that a uniform expansion and contraction of the platinum layer along the entire length of the cilia is sufficient for obtaining non-reciprocal motion in this range of Sperm numbers. Finally, we note that it is possible to design our cilia to have internal

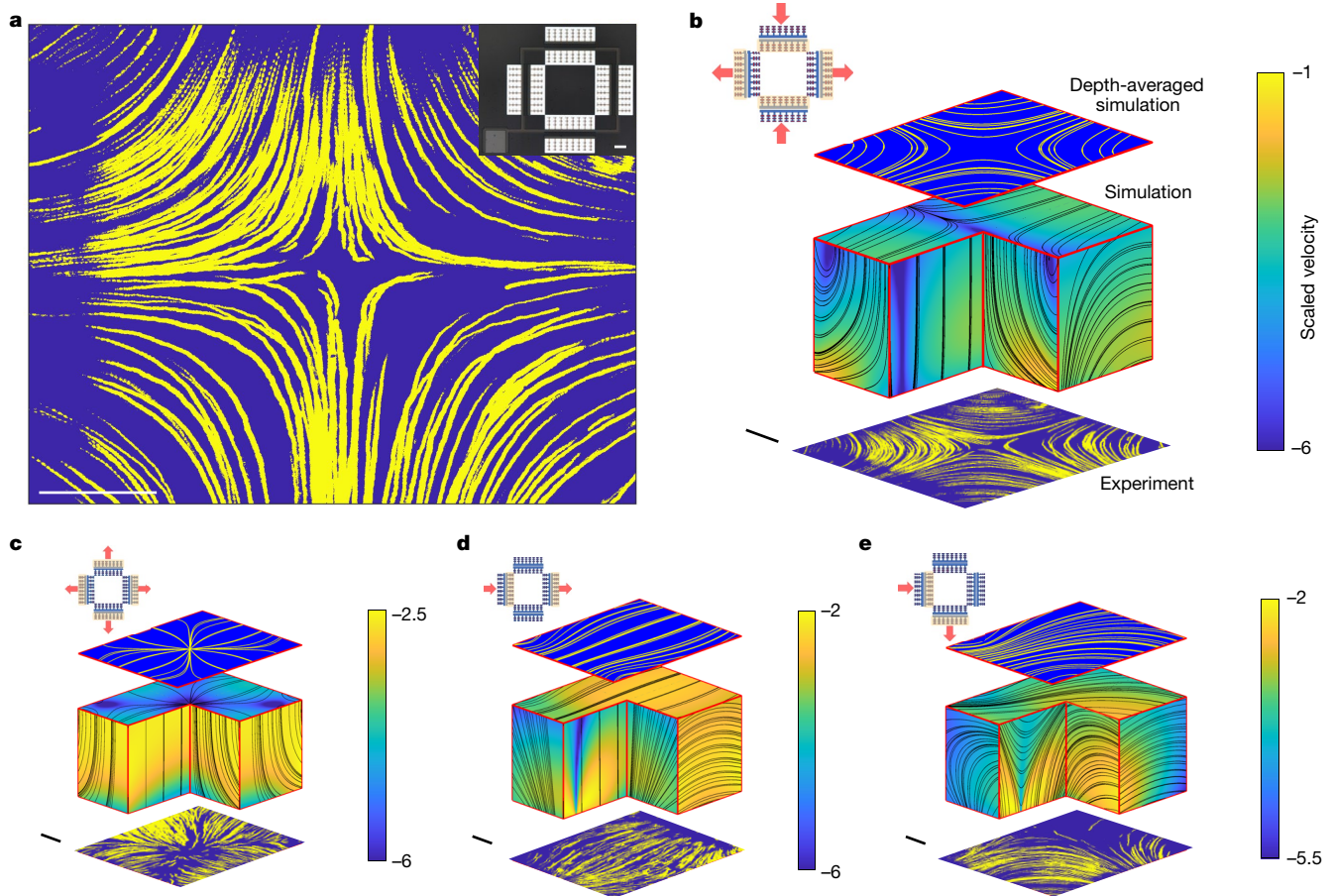


**Fig. 2 | Elementary flow patterns generated by cilia units. a.** An extensional flow generated by a programmable cilia unit. Each unit consists of eight cilia arrays, with each array consisting of eight cilia  $50\ \mu\text{m}$  in length spaced laterally by  $25\ \mu\text{m}$  (shown in inset, top right). The yellow tracks indicate the trajectories of fluorescent particles in the fluid. **b.** 3D flow generated by surface-driven extensional flow. A composite experimental and simulation image showing the extensional flow measured in the experiments from **a** (bottom), the simulated 3D flow geometry projected onto the surface of a  $3/4$  cuboid (middle), and the

simulated flow averaged over the entire depth (top). The scaled velocity in the simulations is  $F/L\mu$  (see Methods for details) and the colour scale indicates the logarithm of the flow magnitude. The upper-left schematic of the cilia unit highlights the active cilia arrays (orange) and resulting flow directions (red arrows). **c–e.** Additional composite experimental and simulation images for expansion (**c**), transport (**d**) and turning (**e**) elementary flow geometries. Scale bars,  $50\ \mu\text{m}$ .

degrees of freedom. Although more complicated, such cilia can break time-reversal symmetry without the need for elastic deformations due to hydrodynamic forces (see Extended Data Fig. 6 and Supplementary Video 4).

This platform can be used to create active cilia metasurfaces that are able to generate and switch between arbitrary flow patterns. To construct these metasurfaces, we fabricate artificial cilia units comprised of independently actuable cilia arrays configured in a square geometry (Fig. 2a, top right). We fabricate two arrays on each side to enable bidirectional pumping. By actuating different cilia arrays to generate flows into or out of the square along different sides, we are able to generate a wide range of elemental surface flow geometries. An illustrative experimentally measured extensional flow pattern is shown Fig. 2a. This image shows the trajectories of fluorescent tracer particles (yellow) transported by the induced flows in a horizontal plane near the cilia tips (see Methods for details of the experimental measurements, and Supplementary Video 5 for a video of induced flow). Although the flows are generated at the cilia metasurface, they extend into the fluid bulk, with a free surface boundary roughly  $1\ \text{mm}$  above the metasurface. To determine the three-dimensional (3D) flows generated by the actuating surface, we perform simulations in which each cilium is modelled by a localized force acting on the fluid (stokeslet<sup>37</sup>; see Methods for

details) and plot the 3D streamlines for heights ranging from  $0.8$  to  $4$  cilia lengths (roughly  $40\ \mu\text{m}$  to  $200\ \mu\text{m}$  above the surface for cilia that are  $50\ \mu\text{m}$  in length). To provide intuition for the generated flows, we present a composite image that illustrates the experiment results, the 3D simulation results depicted in a  $3/4$  cuboid geometry on the external faces of the depicted volume, and the depth-averaged simulation flow pattern (Fig. 2b). In addition, we depict the active cilia arrays in each unit (orange highlights) and the direction of the flows they induce (red arrows). We find excellent correspondence between the simulations and the experiments. Moreover, the simulations clearly show that the cilia, in addition to pumping flows parallel to the metasurface, act as tethering points for drawing in fluid from higher planes into the actuated flows. Additional composite images for expansion, transport, and turning flows are shown in Fig. 2c–e, respectively. Similar patterns are generated when an additional upper boundary is included (see Methods and Extended Data Fig. 7 for details). Collectively, these measurements and simulations illustrate that the cilia units can generate a wide range of elementary flow geometries.

To demonstrate a cilia metasurface can generate arbitrary and switchable flows, we fabricate a fully wired surface with 16 programmable ciliary units, where each of the 64 cilia arrays can be independently controlled. Here, each array is wire-bonded to a single pin of a chip carrier

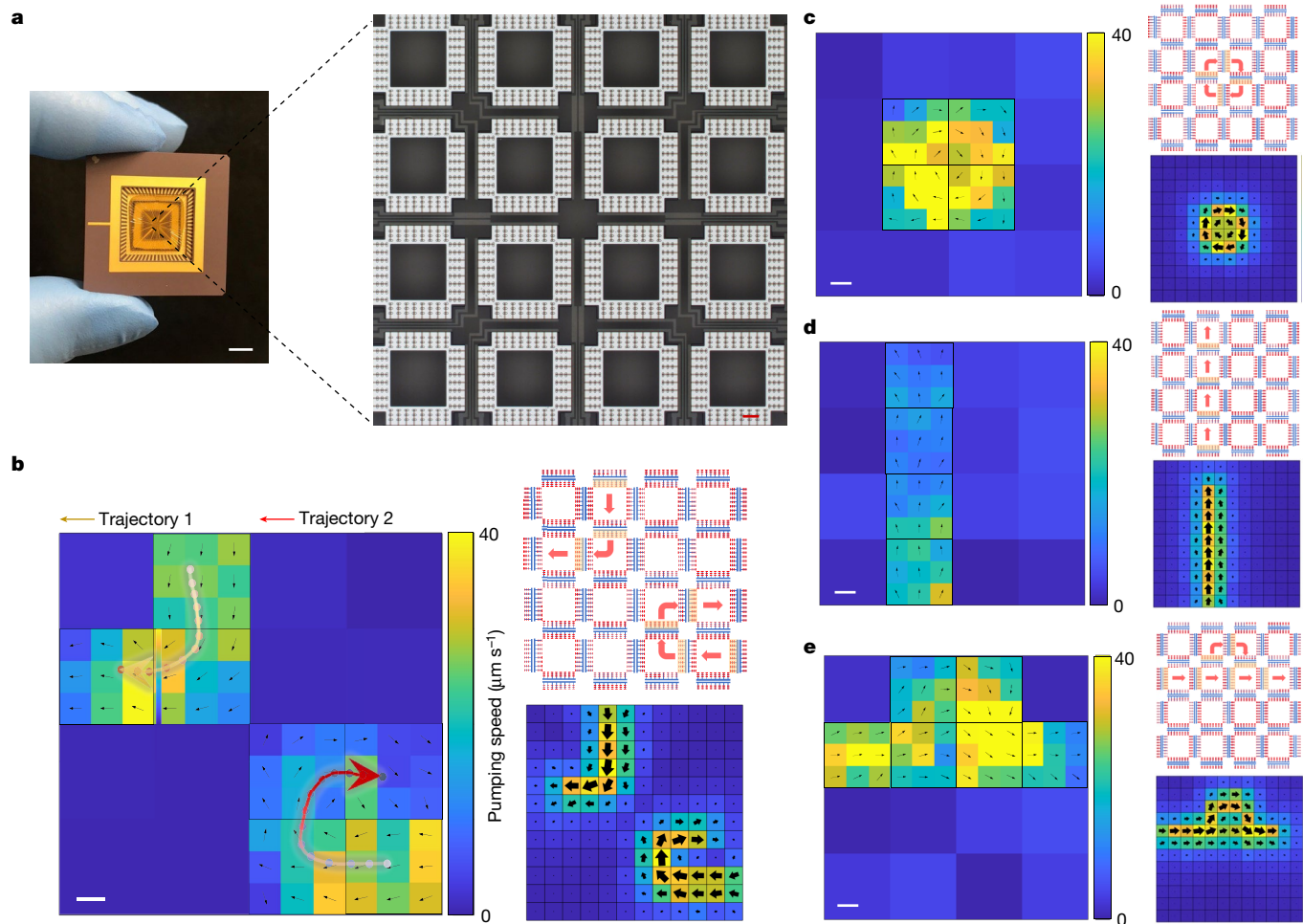


**Fig. 3 | Cilia metasurface capable of generating arbitrary and switchable microfluidic flows.** **a**, The cilia metasurface consists of a chip with  $4 \times 4$  arrays of cilia units. Shown are an image of the chip (left), and the  $4 \times 4$  cilia units tiling (right). The 64 individual cilia arrays are wire-bonded to the chip carrier, which is in turn connected to a data-acquisition device driven by LabVIEW. **b**, Two independent flow trajectories generated by the cilia metasurface. We plot the experimentally measured particle velocimetry data (left), a schematic of the

activated cilia arrays (upper right), and the simulated flow pattern (lower right). For clarity, we also include an individual particle track for each flow trajectory. **c–e**, Additional flow trajectories generated by the cilia metasurface including local rotation (**c**), localized transport across the metasurface (**d**), and trajectories that split and merge (**e**). Scale bars: 5 mm (**a**), 50  $\mu\text{m}$  (**a**, inset), 100  $\mu\text{m}$  (**b–e**).

(ceramic pin grid array (CPGA) or side-brazed dual in-line ceramic package (DIP) package) as shown in Fig. 3a. The voltages of the individual chip carrier pins were controlled via a data-acquisition board driven by LabVIEW (Extended Data Fig. 8). For each flow pattern in Fig. 3b–e we present at left the particle velocity data, plus the designed flow in the upper right, and the simulated flow in the bottom right. In Fig. 3b we demonstrate our ability to drive two independent spatially separated flow trajectories. For further clarity we include an individual particle track for each flow trajectory. Using the same cilia metasurface we are able to drive a wide range of additional flow patterns including localized rotation (Fig. 3c), localized transport across the entire region (Fig. 3d) and trajectories that split and merge (Fig. 3e). In each case, we obtain excellent fidelity between the designed, simulated and experimentally measured flows. Additionally, these flows can be switched on command. As a simple example, we show in Supplementary Video 6 that the rotation direction in Fig. 3c can be reversed. These studies illustrate the vast range of flow manipulations that can be achieved using this platform. To visualize any of the possible flows, we have created a MATLAB application (see Supplementary Code 1) that plots the simulated flows for active cilia array patterns chosen by the user.

A major advantage of these artificial cilia is that they can be integrated with CMOS-based microcircuits for untethered control. We

demonstrate this integration by fabricating a photovoltaic-powered CMOS clock circuit (Fig. 4a) to drive metachronal waves in the cilia arrays (Fig. 4b; see Methods and Extended Data Fig. 9 for fabrication process). The wireless CMOS clock circuit contains over 1,000 transistors and is fabricated by X-FAB Silicon Foundries with a 180-nm node CMOS process on a silicon-on-insulator wafer. It uses a proportional to absolute temperature (PTAT) current source, a relaxation oscillator to generate a clock signal, a frequency divider to select the output frequency, and a phase shifter to get different phases. These components work together to generate a series of phase-shifted voltage signals at a selected frequency when illuminated with light (Fig. 4c and Extended Data Fig. 10a, b). We estimate that for a light intensity of approximately 1 sun ( $1 \text{ kW m}^{-2}$ ) this circuit with 25  $\mu\text{m}$  by 25  $\mu\text{m}$  photovoltaics would provide 140 nA (Extended Data Fig. 10c), which is enough to actuate about 130 cilia at  $1 \text{ V s}^{-1}$ . Further details relating to the clock circuit design and operation can be found in the Methods section. The cilia and interconnects were added via eight layers of lithographic postprocessing. The clock signals were used to drive metachronal waves in the artificial cilia (Supplementary Video 7). Given a separation of about 1.4 cilia lengths between the arrays we expect considerable coupling between the induced flows<sup>38</sup>. Indeed, we find that pumping is optimal when adjacent cilia arrays have a phase

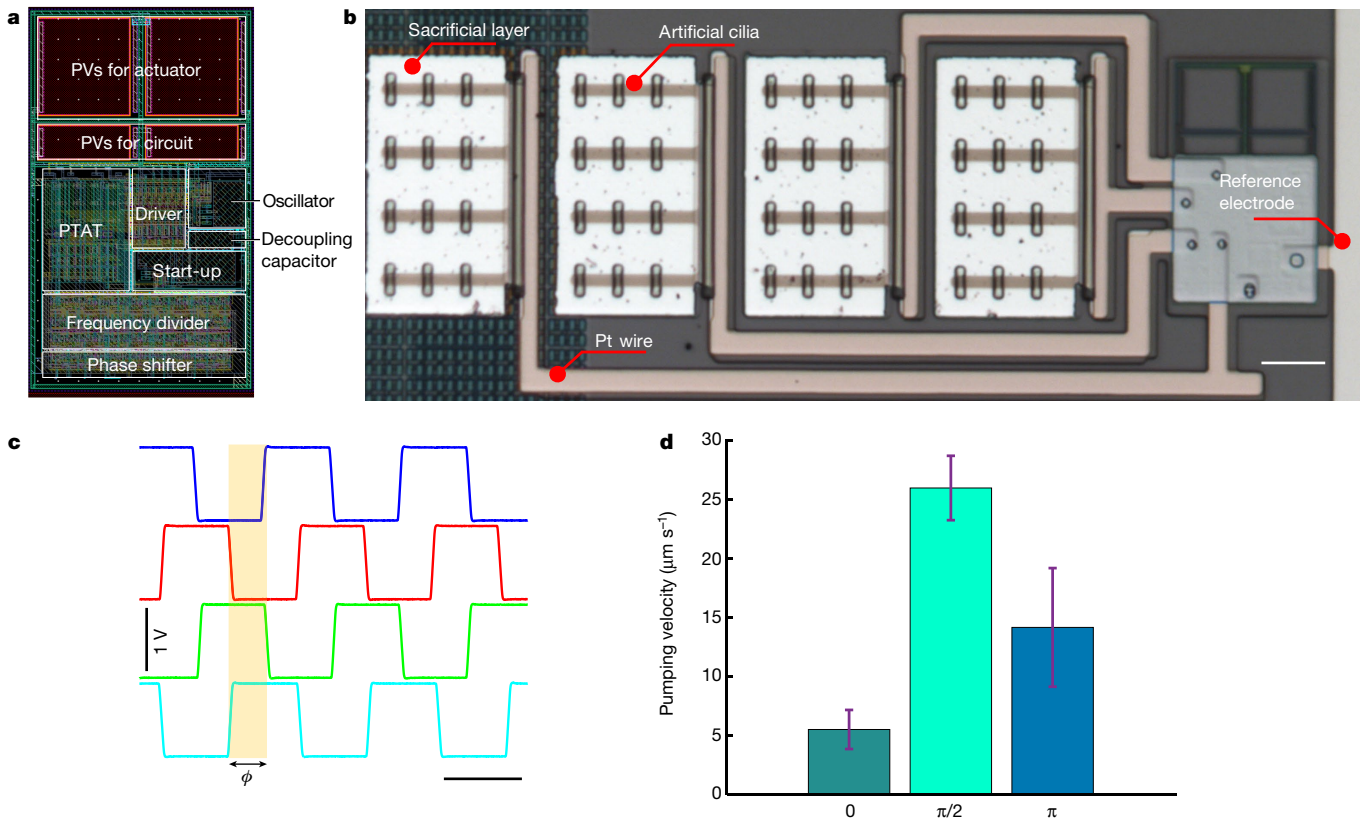


**Fig. 4 | Metachronal waves generated by untethered control of CMOS integrated artificial cilia arrays.** We use a CMOS circuit powered by photovoltaics (PVs) to drive metachronal waves in the artificial cilia. **a**, Circuit layout indicating circuit components. PTAT, proportional to absolute temperature current source. **b**, Optical image of the CMOS circuit integrated with four artificial cilia arrays. **c**, Measurements of four voltage outputs from the CMOS circuit showing a phase delay  $\phi$  of  $\pi/2$  between the voltage pulses

driving the cilia arrays. **d**, Pumping velocity versus phase delay for artificial cilia driven at 16 Hz averaged over five separate measurements. The error bars indicate the standard deviation. We find that a  $\pi/2$  phase delay between the arrays produces a pumping velocity that is approximately 370% higher than that obtained without phase delays, and around 84% higher than that obtained for phase delay of  $\pi$ . Scale bars: 25  $\mu\text{m}$  (**b**), 0.03 s (**c**).

delay of roughly  $\pi/2$  (Fig. 4d), a result that is consistent with prior literature<sup>45</sup>. Furthermore, because non-reciprocal behaviour is built into the  $\pi/2$  clock cycle, this phase delay can enhance non-reciprocal behaviour even at low driving frequencies. More broadly, this result demonstrates the vast potential for untethered control by embedding electronics in this platform.

Collectively, the experiments and simulations presented here forecast the excellent prospects for using this artificial cilia platform to achieve untethered control and arbitrary switchable microfluidic manipulations in aqueous media. For example, optically powered CMOS circuits with integrated sensors could be used to measure the chemical, optical and thermal state of the surrounding fluid, in order to choose the appropriate microfluidic manipulation. As such, we envision a near future where cilia metasurfaces could enable numerous fluidic applications in lightweight devices under simple exposure to the sun.

## Online content

Any methods, additional references, Nature Research reporting summaries, source data, extended data, supplementary information, acknowledgements, peer review information; details of author contributions and competing interests; and statements of data and code availability are available at <https://doi.org/10.1038/s41586-022-04645-w>.

- Thorsen, T., Maerkl, S. J. & Quake, S. R. Microfluidic large-scale integration. *Science* **298**, 580–584 (2002).
- den Toonder, J. M. J. & Onck, P. R. Microfluidic manipulation with artificial/bioinspired cilia. *Trends Biotechnol.* **31**, 85–91 (2013).

- Lee, C.-Y., Chang, C.-L., Wang, Y.-N. & Fu, L.-M. Microfluidic mixing: a review. *Int. J. Mol. Sci.* **12**, 3263–3287 (2011).
- Gu, H. et al. Magnetic cilia carpets with programmable metachronal waves. *Nat. Commun.* **11**, 2637 (2020).
- Wang, Y., den Toonder, J., Cardinaels, R. & Anderson, P. A continuous roll-pulling approach for the fabrication of magnetic artificial cilia with microfluidic pumping capability. *Lab Chip* **16**, 2277–2286 (2016).
- Iverson, B. D. & Garimella, S. V. Recent advances in microscale pumping technologies: a review and evaluation. *Microfluid. Nanofluid.* **5**, 145–174 (2008).
- Blake, J. R. & Sleight, M. A. Mechanics of ciliary locomotion. *Biol. Rev.* **49**, 85–125 (1974).
- Van Houten, J. Two mechanisms of chemotaxis in *Paramecium*. *J. Comp. Physiol.* **127**, 167–174 (1978).
- Sleight, M. A., Blake, J. R. & Liron, N. The propulsion of mucus by cilia. *Am. Rev. Respir. Dis.* **137**, 726–741 (1988).
- Lauga, E. & Powers, T. R. The hydrodynamics of swimming microorganisms. *Rep. Prog. Phys.* **72**, 096601 (2009).
- Lauga, E. Propulsion in a viscoelastic fluid. *Phys. Fluids* **19**, 083104 (2007).
- Satir, P., Heuser, T. & Sale, W. S. A structural basis for how motile cilia beat. *BioScience* **64**, 1073–1083 (2014).
- Sanchez, T., Welch, D., Nicastrò, D. & Dogic, Z. Cilia-like beating of active microtubule bundles. *Science* **333**, 456–459 (2011).
- Zhang, X., Guo, J., Fu, X., Zhang, D. & Zhao, Y. Tailoring flexible arrays for artificial cilia actuators. *Adv. Intell. Syst.* **3**, 2000225 (2020).
- Milana, E. et al. Metachronal patterns in artificial cilia for low Reynolds number fluid propulsion. *Sci. Adv.* **6**, eabd2508 (2020).
- van Oosten, C. L., Bastiaansen, C. W. & Broer, D. J. Printed artificial cilia from liquid-crystal network actuators modularly driven by light. *Nat. Mater.* **8**, 677–682 (2009).
- Li, M., Kim, T., Guidetti, G., Wang, Y. & Omenetto, F. G. Optomechanically actuated microcilia for locally reconfigurable surfaces. *Adv. Mater.* **32**, 2004147 (2020).
- den Toonder, J. et al. Artificial cilia for active micro-fluidic mixing. *Lab Chip* **8**, 533–541 (2008).
- Vilfan, M. et al. Self-assembled artificial cilia. *Proc. Natl Acad. Sci.* **107**, 1844–1847 (2010).
- Khaderi, S. N., den Toonder, J. M. J. & Onck, P. R. Magnetic artificial cilia for microfluidic propulsion. *Adv. Appl. Mech.* **48**, 1–78 (2015).
- Friese, M. E. J., Rubinsztein-Dunlop, H., Gold, J., Hagberg, P. & Hanstorp, D. Optically driven micromachine elements. *Appl. Phys. Lett.* **78**, 547–549 (2001).

22. Zhang, S., Cui, Z., Wang, Y. & den Toonder, J. M. Metachronal actuation of microscopic magnetic artificial cilia generates strong microfluidic pumping. *Lab Chip* **20**, 3569–3581 (2020).
23. Dong, X. et al. Bioinspired cilia arrays with programmable nonreciprocal motion and metachronal coordination. *Sci. Adv.* **6**, eabc9323 (2020).
24. Chen, C.-Y., Chen, C.-Y., Lin, C.-Y. & Hu, Y.-T. Magnetically actuated artificial cilia for optimum mixing performance in microfluidics. *Lab Chip* **13**, 2834–2839 (2013).
25. Miskin, M. Z. et al. Electronically integrated, mass-manufactured, microscopic robots. *Nature* **584**, 557–561 (2020).
26. Liu, Q. et al. Micrometer-sized electrically programmable shape-memory actuators for low-power microrobotics. *Sci. Robot.* **6**, eabe6663 (2021).
27. Purcell, E. M. Life at low Reynolds number. *Am. J. Phys.* **45**, 3–11 (1977).
28. Machin, K. E. Wave propagation along flagella. *J. Exp. Biol.* **35**, 796–806 (1958).
29. Wiggins, C. H. & Goldstein, R. E. Flexive and propulsive dynamics of elastica at low Reynolds number. *Phys. Rev. Lett.* **80**, 3879–3882 (1998).
30. Dreyfus, R. et al. Microscopic artificial swimmers. *Nature* **437**, 862–865 (2005).
31. Khaderi, S. N., Baltussen, M. G. H. M., Anderson, P. D., den Toonder, J. M. J. & Onck, P. R. Breaking of symmetry in microfluidic propulsion driven by artificial cilia. *Phys. Rev. E* **82**, 027302 (2010).
32. Yu, T. S., Lauga, E. & Hosoi, A. E. Experimental investigations of elastic tail propulsion at low Reynolds number. *Phys. Fluids* **18**, 091701 (2006).
33. Lauga, E. *The Fluid Dynamics of Cell Motility* (Cambridge Univ. Press, 2020).
34. Cox, R. G. The motion of long slender bodies in a viscous fluid. Part 1. General theory. *J. Fluid Mech.* **44**, 791–810 (1970).
35. De Canio, G., Lauga, E. & Goldstein, R. E. Spontaneous oscillations of elastic filaments induced by molecular motors. *J. R. Soc. Interface* **14**, 20170491 (2017).
36. Quennou, N., Shelley, M., du Roure, O. & Lindner, A. Transport and buckling dynamics of an elastic fibre in a viscous cellular flow. *J. Fluid Mech.* **769**, 387–402 (2015).
37. Blake, J. R. A note on the image system for a stokeslet in a no-slip boundary. *Math. Proc. Cambridge Philos. Soc.* **70**, 303–310 (1971).
38. Khaderi, S. N., den Toonder, J. M. J. & Onck, P. R. Microfluidic propulsion by the metachronal beating of magnetic artificial cilia: a numerical analysis. *J. Fluid Mech.* **688**, 44–65 (2011).

**Publisher's note** Springer Nature remains neutral with regard to jurisdictional claims in published maps and institutional affiliations.

© The Author(s), under exclusive licence to Springer Nature Limited 2022

## Methods

### Experiments

**Fabrication of artificial cilia.** The fabrication process consists of growing Pt and Ti, etching these layers, and fabricating polymeric panels.

1) A release layer of 180 nm aluminium was deposited on Borofloat glass using a thermal evaporator (CVC SC4500). To protect this release layer during fabrication, an additional 20 nm  $\text{Al}_2\text{O}_3$  was grown at 110 °C using atomic layer deposition (ALD) by Oxford ALD FlexAL. To pattern these release layers, a positive photoresist (Microposit S1813) was spin-coated and exposed using a contact aligner from ABM Industries, and the wafer was then developed in a developer (MicroChemicals AZ 726 MIF). The exposed release layers were etched by an aluminium etchant. Then, the photoresist was stripped by an organic remover (Microposit Remover 1165) with sonication, followed by oxygen plasma clean for 3 min (Oxford PlasmaLab 80+).

2) To fabricate the cilia, 3 nm of Ti was sputtered onto the sample at 3 mTorr and 400 W (AJA sputter tool).

3) Then, a 7-nm Pt layer was grown using ALD (Arradiance GEMStar) at 250 °C.

4) A positive photoresist S1813 was spin-coated, and the cilia pattern was defined by photolithography.

5) The Ti and Pt layers were then etched by an ion mill tool at 600 V (AJA ion mill). Then the photoresist was stripped in the organic remover.

6) A negative photoresist (MicroChemicals NLOF 2020) was spin-coated and patterned as the rigid panels to regulate the deformation of artificial cilia.

7) To balance the prestress in Pt/Ti layers, the top surface of Pt layer was oxidized by 1-min oxygen plasma. This step enables us to control the shape of the cilia upon release so that they do not get damaged during the various fluid-exchange processes.

8) Finally, the sample was baked at 170 °C for 30 min to strengthen the adhesion between the Pt layer and polymer panels.

**Fabrication of cilia metasurface.** Between the aforementioned steps 5) and 6), metal electrodes (10-nm Ti and 60-nm Pt) were patterned to interconnect the cilia to the soldering pads. The chip was then packaged into a chip carrier with a dual in-line ceramic package (DIP; CSB06428D) and ceramic pin grid array (CPGA; CPG06858) from Spectrum using aluminium wires via wire bonding (Westbond 7400A Ultrasonic Wire Bounder) after the fabrication of artificial cilia. Finally, the aluminium wires were protected by optical adhesive (NOA 60, Norland Products).

**Design of the control circuit.** The optically powered CMOS circuits that drive the actuators are designed in Cadence and fabricated by X-FAB Silicon Foundries with a 180-nm node CMOS process. The circuit has two sets of silicon photovoltaics (PVs), one to power the surface electrochemical actuators and one to power the circuit. The electronics consist of a proportional to absolute temperature (PTAT) current source, a relaxation oscillator, a frequency divider consisting of D-type flip-flops that reduces the frequency of the relaxation oscillator to a usable range (approximately 2 Hz to 256 Hz, which can be set by hard-wiring the circuit in post-processing), a phase shifter that produces square waves with a phase offset, and a driver that uses the phase-shifted waves from the circuit to control the voltage applied to the artificial cilia.

**Fabrication of CMOS-integrated artificial cilia.** Integration of CMOS electronics represents a major advance over our previously reported work<sup>25</sup>, in which photovoltaics, in conjunction with a user-guided laser, were used to control actuation. This device was built on the silicon-on-insulator substrate with a CMOS circuit from X-FAB.

1) The  $\text{SiO}_2$  layer on top of the CMOS circuit was first thinned by inductively coupled plasma etching (Oxford PlasmaLab 80+).

2) A 180-nm aluminium (doped with 1% silicon) layer and a 30-nm ALD  $\text{Al}_2\text{O}_3$  layer were deposited and patterned as release layers.

3) The electrical contacts were made by selectively etching the top  $\text{SiO}_2$  layer.

4) Metal wires (10-nm Ti and 60-nm Pt) were patterned to interconnect the CMOS circuit and artificial cilia.

5) A 300-nm silica insulation layer was then patterned on top of the CMOS circuit, preventing short circuits among the circuit, the subsequent layers and the electrolyte.

6) Chrome was deposited and patterned as the light shielding layer on top of the CMOS circuit, leaving only the photovoltaics exposed to light. Finally, the artificial cilia were fabricated following the recipe in Methods subsection 'Fabrication of artificial cilia'.

**SEM imaging.** To obtain the SEM images of the artificial cilia (Fig. 1b), the sample was released from the substrate in 2.38 wt% tetramethylammonium hydroxide (TMAH) aqueous solution. Then, the sample was washed by deionized water and isopropanol sequentially, and dried in a critical point drier (Leica CPD300). Finally, the sample was sputtered with a thin layer of gold, and imaged in an SEM tool (Zeiss Supra 55).

**STEM imaging.** To image the actuator using STEM, 3-nm Ti and 7-nm Pt were grown on a bare silicon wafer. Then, an amorphous carbon protective layer was smeared on top. Then, the top lamina was milled using an ion beam (Thermo Fisher Helios G4 UX FIB). The device was then attached to a copper grid using a nano-manipulator. Finally, we thin the top lamina using a focused ion beam to make it transparent under electrons. The recorded signal is proportional to the mass thickness and atomic number, such that the Pt layer, as the strongest scatterer, showed as white, and the lighter Ti capping layer showed as dark grey.

**Characterization of the actuation and pumping velocity of artificial cilia.** An inverted microscope (Olympus IX71) integrated with a three-axis micromanipulator (Sensapex) and a video camera was used to visualize the actuation of artificial cilia. A Pt/Ir probe coated with parylene was attached to the artificial cilia to apply voltage. An Ag/AgCl electrode was used as the reference electrode. A function generator was used to generate the voltage signals. A video camera was used to capture the actuation of artificial cilia in Fig. 1. To release the cilia from the substrate, the devices were immersed in 2.38% TMAH aqueous solution for several hours to etch the aluminium and  $\text{Al}_2\text{O}_3$  release layers, thereby releasing the cilia into the solution. The cilia were then washed using deionized water several times and transferred into 1× PBS solution. To track the fluid motion, 2- $\mu\text{m}$  polymer tracer particles were added to the solvent. The fluid velocity data reported in this paper are the averaged velocity of the tracked particles. We estimate a measurement error of approximately 20% in the velocity.

**Characterization of the flow patterns generated by an artificial cilia unit.** To obtain high fidelity particle tracks we used 4- $\mu\text{m}$  yellow-green fluorescent particles (FluoSpheres Sulfate Microspheres) in combination with an optical filter. The filter ensures that only the fluorescent particles are visible. The resulting videos were processed using MATLAB to obtain the trajectories of the fluorescent particles shown in the experimental images of Fig. 2.

**Characterization of remotely controlled artificial cilia.** A microscope in reflection mode with a halogen light and red laser (660 nm) with tunable intensity were used to visualize and power the circuit and artificial cilia. A video camera was used to record the actuation of the artificial cilia. The microscale polymer particles were put into the solvent to track the resulting fluid flows.

**Working environments.** Although the measurements reported here were conducted in PBS, the artificial cilia work in a broad range of pH

# Article

conditions ranging from 0.5 to 13.4 (see Supplementary Video 8). Because the redox reaction of Pt only requires a conductive aqueous solution with trace electrolyte ( $\text{Na}^+$ ,  $\text{K}^+$ ,  $\text{Mg}^{2+}$ , and so on), the artificial cilia can be operated in environments ideal for biological/biomedical applications.

**Design of two-hinge cilium.** Importantly, these cilia can be designed to have internal degrees of freedom that can vastly increase the swept area and hence the pumping efficiency. We demonstrate this concept using a cilia design comprised of two hinges that are actuated independently with a phase delay, as shown in Extended Data Fig. 6. The fabrication of these cilia is very similar to the fabrication steps for the single-hinge cilia. Here, however, we include a secondary wire that passes through the first hinge and activates the second hinge (Extended Data Fig. 6a). A 3D rendering of the two-hinge cilium is shown in Extended Data Fig. 6b. Its operation can be characterized by the two hinge angles,  $\theta_{h1}$  and  $\theta_{h2}$ . To maximize the pumping efficiency, we use a geometric calculation to tune the initial and final angles for each hinge so that the swept area over one cycle, which consists of four actuations steps, is maximized (Extended Data Fig. 6c). Assuming equal length panels, the hinge angles at the start of the stroke that maximize the swept area are  $\theta_{h1} = 2.02$  rad,  $\theta_{h2} = 2.23$  rad. We implement this stroke in our fabricated two-hinge cilium and find that the mean pumping distance per cycle is about  $4.9 \pm 0.5$   $\mu\text{m}$  (Extended Data Fig. 6e and Supplementary Video 4). This result is larger compared to the pumping distance reported in the text, which is about 2.9  $\mu\text{m}$  per cycle (Extended Data Fig. 6e). Moreover, the two-hinge cilia can be made much larger and operated at much lower frequencies than their single-hinge counterparts. These results highlight the versatility of our system for creating cilia with internal degrees of freedom.

## Theory and simulations

**Model of a single cilium.** To elucidate the physical mechanism behind the motion of the cilia, we develop a simple theoretical model that captures all the important dynamical features that are experimentally observed. We model a single artificial cilium as a slender, inextensible elastic rod with a centerline  $\mathbf{x}(s, t)$ , at time  $t$ , parameterized by its arc length  $s$ . In the experiments, the motion is driven by expansion/contraction of one side of the cilium caused by chemical reactions due to an applied oscillating electrical potential. We model this forcing as a periodic variation of the natural curvature of the centerline and assume it is uniform along its length

$$\kappa_0(t) = K + A \sin \omega t, \quad (1)$$

where  $A$  and  $K$  are constants and  $\omega$  is the actuation (angular) frequency.

The rest of the model is based on a standard approach for micro-sized slender, elastic filaments immersed in a viscous fluid, at low Reynolds number<sup>39</sup>. The elastic forces are computed using a classical Kirchhoff rod model (linear elasticity) with prescribed natural curvature<sup>40</sup>, whereas the hydrodynamic forces are based on the standard resistive force theory of slender filaments<sup>34</sup> that assumes that the drag force density  $f_h(s)$  is local and anisotropic and can be found as

$$f_h(s) = -(\xi_{\parallel} \mathbf{t} \mathbf{t} + \xi_{\perp} \mathbf{n} \mathbf{n}) \cdot \frac{\partial \mathbf{x}}{\partial t}, \quad (2)$$

where  $\mathbf{n}$  and  $\mathbf{t}$  are a local unit normal and a tangent to the centerline, and  $\xi_{\perp} = 2\xi_{\parallel}$  are the drag coefficients in the said directions.

For the boundary conditions, we assume that the rod is clamped at one end ( $s = 0$ ) and that there is no force or torque applied at the other end ( $s = L$ ). For simplicity, we non-dimensionalize the governing equations by scaling length by the length of a cilium  $L$ , time by the elasto-hydrodynamic timescale  $\tau = \xi_{\perp} L^4 / B$ , where  $B$  is the elastic bending modulus of the effective cross-section that we assume is constant in time and uniform along the length. Also, as we assume that the shape

remains two-dimensional, it is most convenient to use the tangential angle  $\theta(s, t)$ , which is the angle between a local tangent to the centerline and the clamping direction at the fixed end.

Finally, the model is then described by the following set of equations

$$\theta_t = -\theta_{ssss} - 3\Lambda_s \theta_s + (-\Lambda + 2\kappa_0 \theta_s + 9\theta_s^2) \theta_{ss}, \quad (3)$$

$$\Lambda_{ss} - \frac{1}{2} \theta_s^2 \Lambda = 3\theta_{ss}^2 + \left(2\kappa_0 + \frac{7}{2} \theta_s\right) \theta_{sss} + \frac{1}{2} (\kappa_0 - \theta_s) \theta_s^3, \quad (4)$$

with boundary conditions

$$\theta(0, t) = 0; \theta_s(1, t) = \kappa_0(t); \theta_{ss}(1, t) = 0; \Lambda(1, t) = 0, \quad (5)$$

$$\theta_{sss}(0, t) + \theta_s(0, t) [\Lambda(0, t) + (\kappa_0 - \theta_s) \theta_s] = 0, \quad (6)$$

$$\Lambda_s(0, t) - (2\kappa_0 + 3\theta_s) \theta_{ss} = 0, \quad (7)$$

where  $\Lambda(s, t)$  is a Lagrange multiplier that ensures the inextensibility of the centerline and letters in subscript denote a partial derivative with respect to the variable written in the subscript.

The governing equations (equations (3), (4)) represent the local balance between the viscous drag and the internal elastic forces<sup>40</sup>, algebraically manipulated to be most suitable for numerical simulations<sup>36</sup>. The boundary conditions shown in equation (5) are those imposed by the assumptions that the root ( $s = 0$ ) is clamped in a fixed direction and the tip ( $s = 1$ ) is free of any external forces and moments and thus, as we are in the inertia-less limit, free of any internal forces and moments. The remaining boundary conditions (equations (6), (7)) represent the vanishing elastic force density at the root. The elastic force vanishes because it is balanced by the viscous drag, which vanishes because the root is not moving.

Besides the initial shape of the centerline and the dimensionless mean and amplitude of the natural curvature ( $K$  and  $A$  in equation (1)), the evolution of the model centerline depends on the above-mentioned dimensionless Sperm number  $\text{Sp} = (\omega \tau)^{1/4} = L(\omega \xi_{\perp} B^{-1})^{1/4}$ . In terms of the equations, the Sperm number comes in through the natural curvature forcing as its dimensionless frequency.

The equations are evolved in time by a backward time-stepping scheme as described in ref.<sup>36</sup>. Results of an example simulation with  $\text{Sp} = 2.8$ ,  $K = A = 1.1$  are shown in Fig. 1h. The relationship between pumping efficiency and Sperm number is shown in Extended Data Fig. 4c.

**Flow simulations.** To simulate the flow, averaged over a fast beating period, we model each cilium as a point force of strength  $F$ , acting on the surrounding fluid. The flow of a point force is adjusted for the presence of a rigid surface to which the cilia are attached<sup>37</sup>. To best capture the time-averaged flow, point forces are placed at height of  $0.7L$  above the substrate, where  $L$  is the length of a cilium. The value was chosen based on the average height above the surface of the tip of a cilium throughout its beat. Throughout the paper, we present the results of flow simulations as dimensionless velocities, non-dimensionalized by the typical velocity of the model  $F/L\mu$ , with  $\mu$  the dynamical viscosity of the surrounding fluid.

Owing to the linearity of the Stokes equations that describe the motion of the fluid, we obtain the full model flow by superposition of all the point-force flows that model each actuated mechanical cilium. We compute the flow on a rectangular grid of points with a horizontal footprint similar to the field of view of the experiments, whereas the vertical coordinate ranges from  $0.8L$  to  $4L$ . For the illustrations of 2D streamlines compared to the experiments, we formulate a compressible 2D flow by averaging the 3D flow along its height above the surface.

Finally, we determine whether such elementary flows can be generated when there is an additional boundary parallel to the substrate. The flow due to a point force can be approximated in this case<sup>41</sup>. The leading



order of the flow, averaged over the wall-to-wall distance, is parallel to the walls and has the same streamline structure for any value of the channel height. However, this leading-order flow is singular near the horizontal locations of the active cilia, so we regularize the singularities<sup>42</sup> by an algebraic blob of size 0.45 cilia lengths.

### Data availability

All data needed to evaluate the conclusions in the paper are present in the paper or the Supplementary Information. Source data are provided with this paper.

### Code availability

All code needed to evaluate the conclusions in the paper are present in the paper or the Supplementary Information.

39. Powers, T. R. Dynamics of filaments and membranes in a viscous fluid. *Rev. Mod. Phys.* **82**, 1607–1631 (2010).
40. Audoly, B. & Pomeau, Y. *Elasticity and Geometry: From Hair Curls to the Non-linear Response of Shells* (Oxford Univ. Press, 2010).
41. Liron, N. & Mochon, S. Stokes flow for a stokeslet between two parallel flat plates. *J. Eng. Math.* **10**, 287–303 (1976).
42. Cortez, R. The method of regularized stokeslets. *SIAM J. Sci. Comput.* **23**, 1204–1225 (2001).

**Acknowledgements** We thank D. Koch, B. Bircan, K. Dorsey, T. Ma, T. Pearson, S. Norris and Y. Yang for discussions, and T. Pennell, J. Clark, V. Genova and G. Bordonaro for technical support. This work was supported by the Army Research Office (ARO W911NF-18-1-0032), the National Science Foundation (EFMA-1935252), the Cornell Center for Materials Research (DMR-1719875), the Air Force Office of Scientific Research (MURI: FA9550-16-1-0031), and the Kavli Institute at Cornell for Nanoscale Science. This project has also received funding from the European Research Council under the European Union's Horizon 2020 Research and Innovation Programme (grant no. 682754) and from Trinity College, Cambridge (IGS scholarship). This work was performed in part at Cornell NanoScale Facility, an NNCI member supported by NSF Grant NNCI-2025233.

**Author contributions** W.W., Q.L., M.Z.M. and I.C. conceived the experiments. W.W. and Q.L. designed and fabricated the surface electrochemical actuators, carried out the experiments, and collected and analysed the data. Q.L., W.W., M.F.R. and M.Z.M. developed the fabrication procedure for the platinum actuator. M.C.C., Q.L. and D.A.M. conducted the STEM imaging. A.J.C., M.F.R. and A.C.M. designed the CMOS clock circuit. W.W., Q.L. and M.F.R. determined the fabrication procedure for integrating the CMOS and surface electrochemical actuators. I.T. and E.L. conducted all of the simulations to determine the flow trajectories. W.W., I.T., E.L., P.L.M. and I.C. wrote the manuscript with contributions from all authors.

**Competing interests** The authors declare no competing interests.

### Additional information

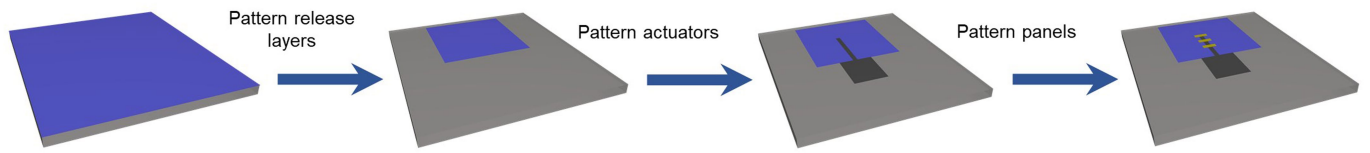
**Supplementary information** The online version contains supplementary material available at <https://doi.org/10.1038/s41586-022-04645-w>.

**Correspondence and requests for materials** should be addressed to Wei Wang, Qingkun Liu or Itai Cohen.

**Peer review information** *Nature* thanks the anonymous reviewers for their contribution to the peer review of this work. Peer reviewer reports are available.

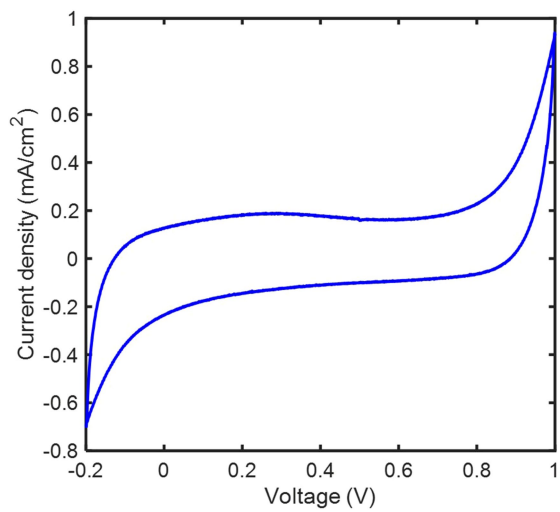
**Reprints and permissions information** is available at <http://www.nature.com/reprints>.

# Article

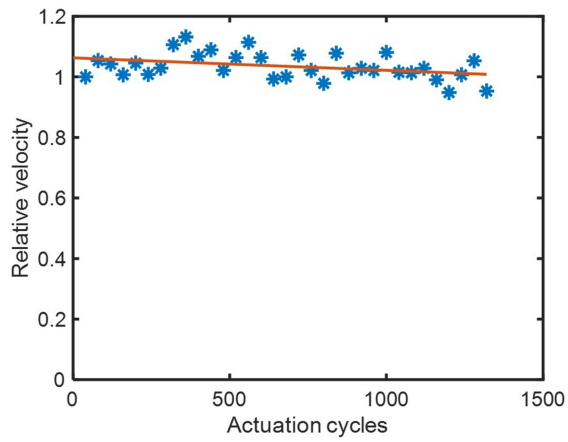


**Extended Data Fig. 1 | Fabrication process of an artificial cilium.** 180-nm Al and 20-nm  $\text{Al}_2\text{O}_3$  were first grown and patterned as the release layer. 3-nm Ti and 7-nm Pt were then grown and patterned as the actuator. Finally, several

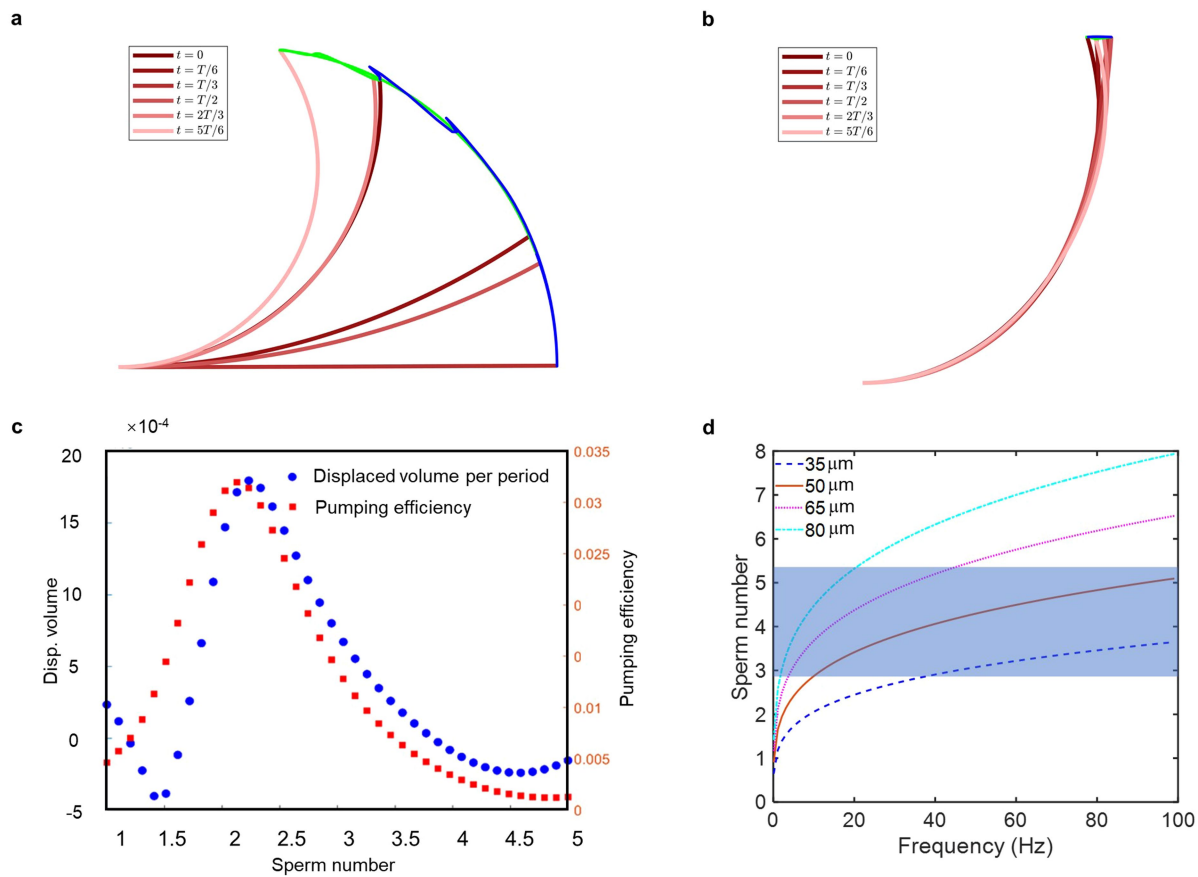
polymer panels were patterned on the actuator to prevent twisting of the cilium.



**Extended Data Fig. 2 | Cyclic voltammetry of artificial cilia.** The cyclic voltammetry curve for an artificial cilium actuated between  $-0.2$  V to  $1$  V at a sweep rate of  $1 \text{ V s}^{-1}$ , the peak current density is about  $1 \text{ mA cm}^{-2}$ .



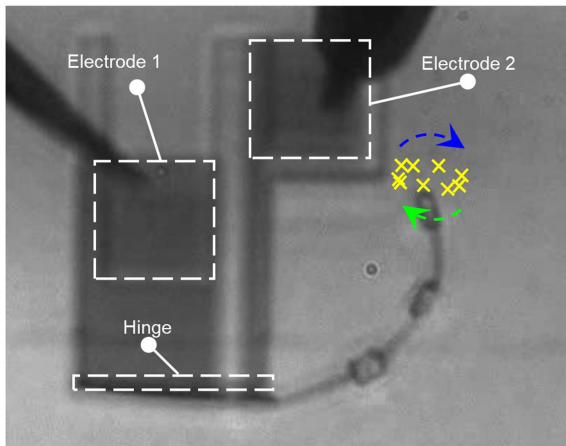
**Extended Data Fig. 3 | Durability of artificial cilia.** Shown is the relative velocity versus the number of actuation cycles. The relative velocity is scaled by the initial pumping velocity. We find no obvious decay after 1,000 actuation cycles. The linear fit to the data indicates that the relative velocity will decrease by 50% after approximately 20,000 actuation cycles.



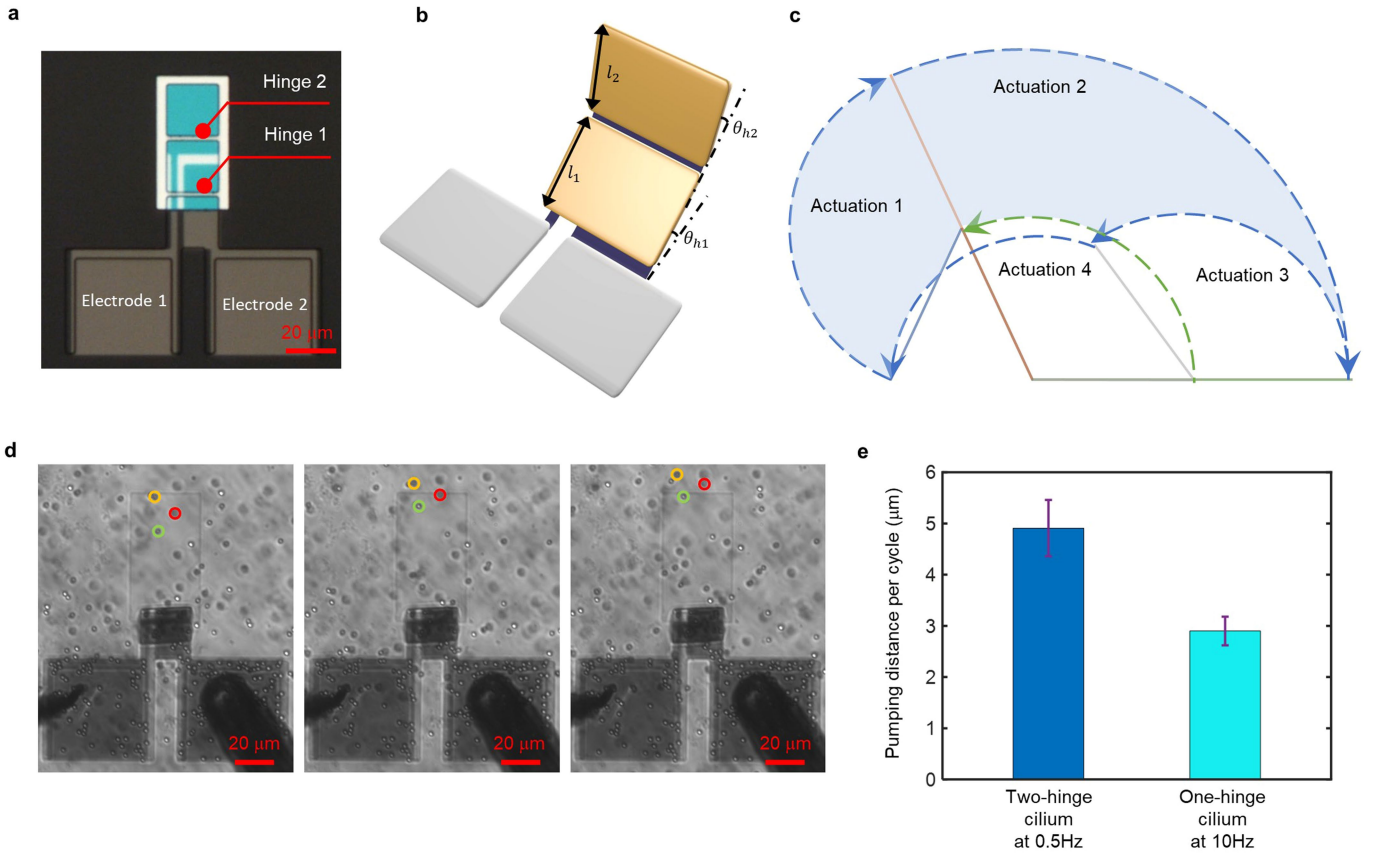
**Extended Data Fig. 4 | Pumping efficiency in simulation and experiment.**

**a**, A cilium beating at around 1 Hz, corresponding to a Sperm number of 1. At these low Sperm numbers, the viscous force is not large enough to break the actuation symmetry. **b**, A cilium beating at around 230 Hz, corresponding to a Sperm number of 7. At these high Sperm numbers viscous drag is too large, diminishing the motion of the cilia. **c**, The relationship between pumping

efficiency, displaced volume, and Sperm number. The pumping efficiency is defined as the ratio between the area covered by the cilium tip and the square of the length of cilium. **d**, The relationship between Sperm number and the actuation frequency for cilia with different lengths. The blue shaded region roughly indicates the maximal pumping velocities measured in the experiments.

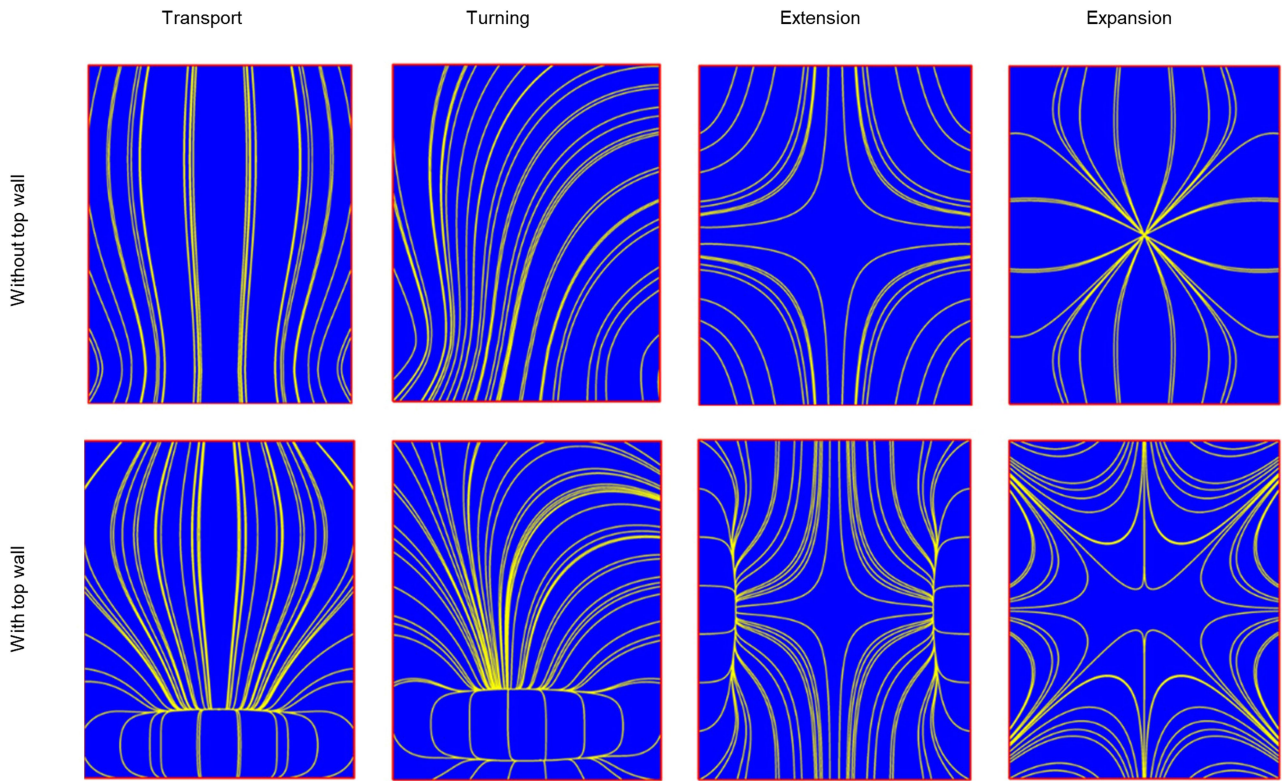


**Extended Data Fig. 5 | A microscopic device for measuring the trajectory of one cilium.** We at first apply a fixed voltage on the hinge through electrode 1 to make the hinge bend up to about  $90^\circ$ , then apply another oscillating voltage through electrode 2 to actuate the cilium.



**Extended Data Fig. 6 | Two-hinge cilium.** **a**, Optical image of a fabricated two-hinge cilium. **b**, A 3D rendering of the two-hinge cilium that defines the segment lengths and hinge angles. **c**, The actuation sequences that maximize swept area (blue shaded region) for the two-hinge cilium. **d**, The positions of several representative particles (marked with yellow, red, and green circles)

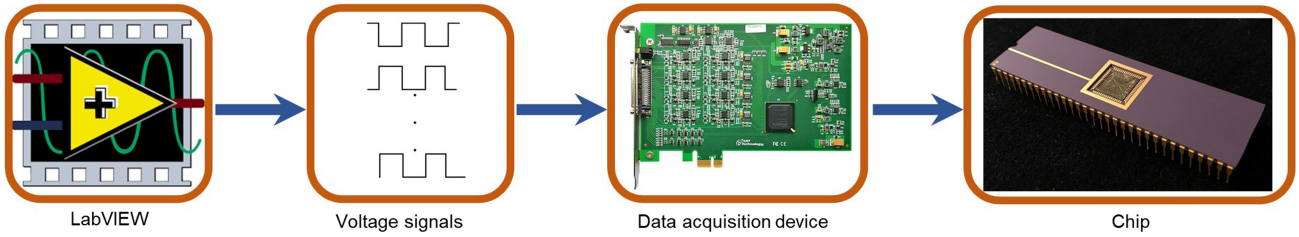
after 0, 1 and 2 cycles of actuations (from left to right). **e**, The pumping distance per cycle for a two-hinge cilium operating at 0.5 Hz and a one-hinge cilium operating at 10 Hz. The data show the mean pumping distance averaged over five separate measurements. The error bars indicate the standard deviation. Scale bars, 20  $\mu\text{m}$ .



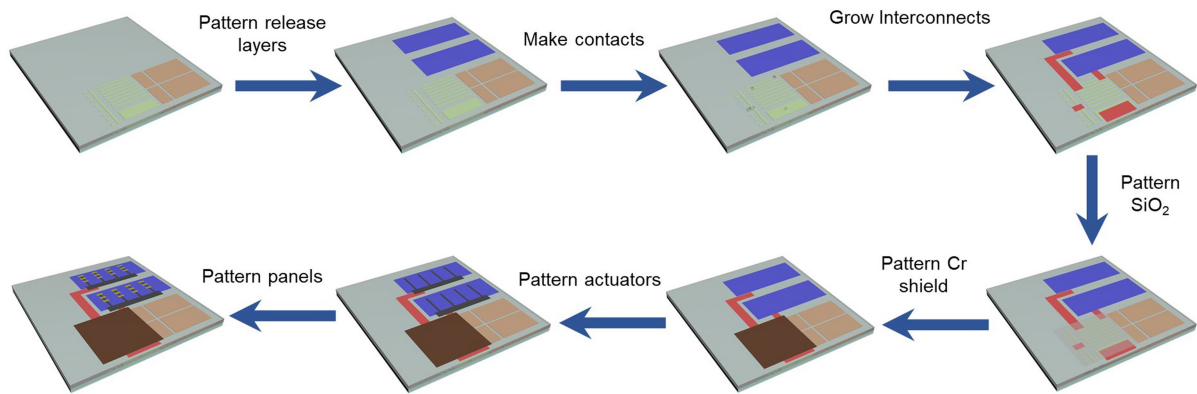
**Extended Data Fig. 7 | Comparison of the streamlines for various cilia activation patterns.** Included are open channels without a top wall (top) and closed channels with a top wall (bottom). All the figures are obtained through numerical simulations. We find that the qualitative features of the streamlines are preserved when the top wall is added. The parts of the streamlines that

deviate from the single-wall case the most are located exactly where the regularized singularities are located, and therefore where the simulation error is largest. The biggest change occurs for the expansion flows, which are inherently 3D. These simulation results suggest thus that the tessellation idea will work in a channel geometry as well.



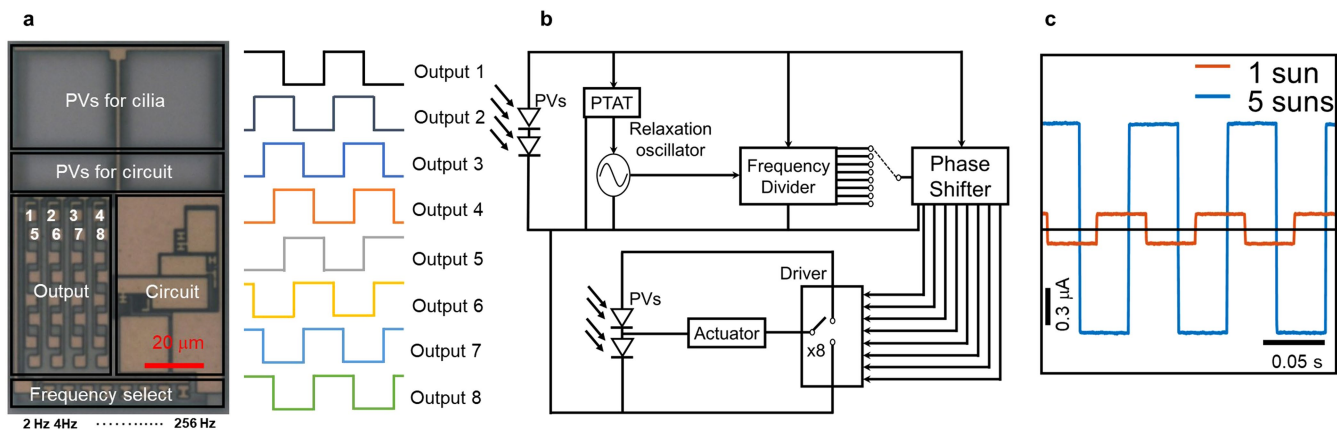


**Extended Data Fig. 8 | An experimental set-up of computer-controlled cilia metasurface chip.** We used a LabVIEW programme to generate voltage signals and send these signals to the data-acquisition device. The output of the data-acquisition device was connected to the cilia metasurface through a breadboard and a chip carrier.



**Extended Data Fig. 9 | Fabrication process for untethered artificial cilia integrated with CMOS circuit.** The orange and yellow zones represent the photovoltaics and the output pins that are used to set the frequency and interconnect to the cilia. Both structures are prefabricated by X-FAB. 180-nm Al and 30-nm Al<sub>2</sub>O<sub>3</sub> were first grown and patterned as the release layers. The metal

contacts were then etched and exposed. Ti/Pt interconnects were patterned to wire the contacts. A protective SiO<sub>2</sub> layer was grown and patterned to prevent electrical shorts and current leaks. A Cr shielding layer was fabricated to protect the circuit from the light. Actuator layers that consist of Ti and Pt were grown and patterned. Finally, polymer panels were patterned on the actuator.



**Extended Data Fig. 10 | CMOS circuit. a**, An optical image of the integrated circuit. The circuit outputs up to eight square waves with phase delays to drive the actuators. We set the frequency by hard wiring, the available frequency ranges from 2 Hz to 256 Hz. **b**, Block diagram of the circuit. **c**, Current versus

time outputs from the circuit under different light intensities. The output current ranges from 140 nA under a light intensity of  $1 \text{ kW m}^{-2}$  equivalent to 1 sun, to about 880 nA at a light intensity of 5 suns. Scale bars: 20  $\mu\text{m}$  (a), 0.3  $\mu\text{A}$  (c, vertical), 0.05 s (c, horizontal).